A new, global optical sediment trap calibration

Authors: M.L. Estapa[1*], C.A. Durkin[2], W.H. Slade[3], C.L. Huffard[2], S.P. O'Neill[1], M.M. Omand[4]

[1] School of Marine Sciences, Darling Marine Center, University of Maine, Walpole, ME, USA
[2] Monterey Bay Aquarium Research Institute, Moss Landing, CA, USA
[3] Sequoia Scientific, Inc., Bellevue, WA, USA
[4] Graduate School of Oceanography, University of Rhode Island, Narragansett, RI, USA

[*] *Corresponding author:* margaret.estapa@maine.edu

Abstract

Autonomous sensors for gravitational carbon flux in the ocean are critically needed, because of uncertainties in the projected response of the biological carbon pump (BCP) to climate change, and the proposed, engineered acceleration of the BCP to sequester carbon dioxide in the ocean. Optical sediment trap (OST) sensors directly sense fluxes of sinking particles in a manner that is independent of, and complementary to, other autonomous, sensor-derived estimates of BCP fluxes. However, limited intercalibrations of OSTs with traditional sediment traps and uncharacterized, potential biases have limited their broad adoption. A global field dataset spanning 3 orders of magnitude in carbon flux was compiled and used to develop empirical models predicting particulate organic carbon flux from OST observations, and intercalibrating different sensor designs. These data provided valuable constraints on the uncertainty in the predicted carbon flux and showed a quantitative, theoretically consistent relationship between observations from OSTs with collimated and diffuse optical geometries. While not designed for this purpose, commercial beam transmissometers have been used as OSTs, so two models were developed quantifying the biases arising from the transmissometer's housing geometry and optical beam diameter. Finally, an algorithm for the quality control of beam transmissometer-derived OST data was optimized using sensitivity tests. The results of this study support the expansion of OST-based gravitational carbon flux measurements and provide a framework for interpretation of OST measurements alongside other gravitational particle flux observations. These findings also suggest key features that should be included in designs of future, purpose-built OST sensors.

1. Introduction

The ocean's biological carbon pump (BCP) plays a key role in regulating Earth's climate by transferring biologically-derived carbon to the ocean's interior, thereby setting the vertical dissolved inorganic carbon (DIC) gradient (Volk and Hoffert 1985). The gravitational carbon pump (GCP), in which particulate organic carbon (POC) passively sinks away from the euphotic zone, is thought to make up about half of the total BCP flux globally (Boyd et al. 2019). Sinking particles in the ocean form through a variety of biological and physical processes which are closely tied to the surface ocean ecosystem state (De La Rocha and Passow 2007; Siegel et al. 2016). Changes in the efficiency of the BCP could lead to climate feedbacks that are poorly constrained at present by Earth system models (Henson et al. 2022). Limited observations of biological carbon fluxes in the global ocean present a key obstacle to improved predictions. In particular, model improvements require observations of biological carbon flux that differentiate key mechanisms of the GCP, and these observations have traditionally required labor-intensive, ship-based methods. In addition, the responsible implementation of marine carbon dioxide removal (mCDR) through nutrient addition to the ocean (e.g., as proposed by National Academies of Sciences, Engineering, and Medicine 2021) will require the rapid deployment of accurate GCP flux sensors that are able to operate independently of ships.

A growing network of autonomous ocean-observing platforms now provides estimates of total BCP fluxes through geochemical budgets of DIC, nitrate, and oxygen, but these estimates do not distinguish the contribution of the GCP (Nicholson et al. 2008; Johnson et al. 2017; Huang et al. 2022). Profiling platforms that measure optical backscattering (b_{bp}) provide POC flux estimates by measuring change in the depth-integrated POC inventory vs. time (Dall'Olmo and Mork 2014), and are calibrated using a broad global dataset of POC:b_{bp} measurements (e.g., Cetinić et al. 2012). This method cannot distinguish sinking from suspended particles under steady-state conditions, or constrain fluxes below the profile depth, but the simplicity and robustness of optical backscattering sensors permit its broad application (Briggs et al. 2011; Alkire et al. 2012; Dall'Olmo and Mork 2014; Bol et al. 2018; Lacour et al. 2019; Giering et al. 2020a; Briggs et al. 2020).

Occasionally, profiling floats equipped with beam transmissometers (Bishop et al. 2004; Bishop and Wood 2009; Estapa et al. 2013, 2017, 2019b) or upward-looking cameras (Bishop et al. 2016; Bourne et al. 2019, 2021) are used as optical sediment traps (OSTs), providing proxy measurements that are specific to gravitational POC flux and can be used under steady-state conditions. In the OST method, sinking particles are intercepted by the sensor itself (the upward-facing optical window of a vertically mounted transmissometer or camera) and the rate of change in the measured light attenuance provides the proxy for flux. However, the direct intercalibration of an OST with a co-deployed, traditional sediment trap is labor-intensive and only two published datasets are available, for the subtropical North Atlantic Ocean (Estapa et al. 2017) and the California Coastal Current (Bourne et al. 2019).

Here, we comprehensively evaluate the performance of the OST method and provide a global calibration, with a goal of broadening the user base of the method, as the need for well-calibrated POC flux measurements grows. We compile a global set of paired attenuance and sediment trap POC flux data from multiple sources spanning contrasting ocean biogeochemical settings, from

the oligotrophic subtropics to the North Atlantic spring bloom. We describe an updated algorithm used for retrieval of attenuance flux from a timeseries of OST measurements, and then present attenuance data that have been derived from two sensor types: *in situ* beam transmissometers, which measure the attenuance of collimated light using a non-imaging sensor as described above; and laboratory photomicrographs of polyacrylamide gel sediment traps (Durkin et al. 2021) from which a mean estimate of uncollimated, diffuse attenuance can be derived (described below). We compare these data to published, diffuse attenuance and POC flux observations described by Bourne et al. (2019), and by Huffard et al. (2020). Taken together, these data provide POC flux calibrations for OST-like beam attenuance and diffuse attenuance sensors, that can be extrapolated broadly in the global ocean. We explore the uncertainties associated with the use of different OST sensor types for POC flux measurements, and finally, we discuss the implications of the relationship between beam attenuance and diffuse attenuance for the design of improved sinking particle flux sensors.

2. Materials and Procedures

2.1. Measurement principles

The term attenuance (*atn*) is used here to refer to the negative log-transformed ratio of the light passing through a plane to a detector (I_d), to the light incident upon that plane (I_o; Equation 1, Figure X).

$$atn = -ln\left(\frac{I_d}{I_o}\right) \qquad [m^2\ m^{-2}] \qquad \text{(Eq. 1)}$$

Note that *atn* as used here follows the definition of Bishop et al. (2016) and is analogous to absorbance (Abs) as defined by Mobley (2022), who instead defined *attenuance* as I_d/I_o. If the light source is collimated and the detector acceptance angle is close to 0° (subject to practical limitations in reality; Boss et al. 2009) then we specify that *atn* is the beam attenuance (atn_c), which is related to the more familiar beam attenuation coefficient (c) of light passing through a sample volume over the pathlength L (Eq. 2a, 2b)

$$c = -\frac{\ln\left(\frac{I_d}{I_o}\right)}{L} \quad [m^{-1}]; \quad atn_c = c \times L \ [m^2\ m^{-2}] \qquad \text{(Eq. 2a, 2b)}$$

where the sampled area of atn_c and the sampled volume of c are related by L. While *atn* is a unitless quantity and c has units of m^{-1}, it is helpful to think of both as ratios, in the case of *atn* between the sample's total attenuance cross section (σ_c, units of m^2; Mobley, 2022) and the sensor's illuminated area (m^2), and in the case of c between σ_c and the volume illuminated by the sensor (m^3). Thus, *atn* has units of $[m^2\ m^{-2}]$, where the numerator refers to the attenuance cross section of the light-attenuating material and the denominator to the geometric area. The attenuance cross section of a single particle can be thought of as the particle's cross sectional area multiplied by the summed fractions of incident light absorbed and scattered by that particle. A particle that is completely opaque, and large relative to the wavelength of the light, will have an attenuance cross section that is twice the geometric cross section of that particle (Mobley 2022).

It is also useful to define a second variant of *atn* for the situation where the illuminating light source is uncollimated and the detector has a wide acceptance angle. This is the case if *atn* is measured using a camera (Bishop et al. 2016; Bourne et al. 2019, 2021). Here, we adopt the name atn_{Kd} which is analogous to the downward, diffuse attenuation coefficient K_d. Similar to the relationship between *c* and K_d in the water column (Mobley 2022), for the same sample we expect atn_c to always be greater than atn_{Kd} because the former excludes more of the scattered light from the detector. As the incident light field becomes less and less diffuse, the value of atn_{Kd} is expected to approach that of atn_c.

The rate of change of *atn* with respect to time serves as the proxy for particle flux (F_{atn}; Eq. 3).

$$F_{atn} = \frac{datn}{dt} \qquad [m^2\ m^{-2}\ d^{-1}] \qquad \text{(Eq. 3)}$$

The proxy assumes that *atn* is only changing due to the accumulation of sinking particles, and not due to transient passage of zooplankton, changes in the background optical properties due to vertical motion of the sensor through the water column, or changes in the background pixel brightness across an image. Therefore, some pre-processing of *atn* data is usually required prior to estimation of F_{atn}. Below, we describe the general methods we have developed to remove interferences from two types of *atn* data: 1) timeseries of atn_c collected using beam transmissometers used as OSTs on autonomous floats drifting at a sampling depth; and 2) atn_{Kd} computed from images of particles accumulated in sediment traps.

2.1.1. Processing atn_c data from in situ transmissometer as OST

A beam transmissometer (C-Rover 2000, 650 nm, 0.25 m pathlength, Sea-Bird Scientific, Bellevue, Washington, USA) deployed as an OST on a drifting autonomous platform returned measurements of sensor depth (*z*), time (*t*), and atn_c at intervals of 3, 5, or 15 minutes, collected over drift periods of 2-6 days (see section 2.3 for descriptions of different data sets presented here). If a rapid sequence of atn_c measurements was collected at each timepoint (i.e., "burst sampling"), these were averaged and timepoints with a standard deviation greater than 0.0013 m^{-2} m^2 were discarded. Points collected outside of ± 25 m from the targeted depth were also discarded. Spikes, which Estapa et al. (2017) observed to be well-correlated with zooplankton swimmer intrusion to nearby sediment traps, were removed from the data using a moving median filter followed by a moving mean filter (Briggs et al. 2011) with a 1.5 h window. As described by Estapa et al. (2017), the despiked data typically contained periods with slowly-increasing atn_c interrupted by rapid increases, and sometimes decreases, in atn_c over a single sampling interval. While we interpret rapid increases as sinking particle flux (see sections 2.2.3 and 3.2.3), rapid decreases can only be explained by loss of accumulated material from the sampling surface, possibly due to turbulence or zooplankton consumption (Estapa et al. 2017). Losses of atn_c at a rate more negative than -0.05 m^2 m^{-2} d^{-1} were therefore cumulatively removed from the data series. After these corrections, the data series were smoothed with a centered, moving mean filter with a 1.5 h window, and the first difference with respect to time computed to obtain F_{atnc} (Eq. 3). Finally, a single mean F_{atnc} value was averaged for the whole drift period for comparison to simultaneously collected sediment trap POC fluxes (see below). A Matlab (Mathworks, Natick, Massachusetts, USA) script carrying out the above steps is also provided (Estapa 2023).

2.1.2 Processing atn_{Kd} data from sediment trap imagery

The majority of the images of sinking particles reported in this study were obtained through laboratory microscopy of polyacrylamide gel collectors that were deployed in cylindrical sediment traps as described by Durkin et al. (2021). Here we describe the image processing procedure to derive a mean value of atn_{Kd} for each gel. Similar image processing procedures were followed to obtain atn_{Kd} from the in situ "Sedimentation Event Sensor" (SES; McGill et al. 2016) camera dataset described in section 2.3.2. Briefly, polyacrylamide gel is a clear, viscous fluid placed in the bottom of a sediment trap, that preserves sinking particle morphology until samples can be imaged under a microscope in the laboratory. Here, the gel samples were imaged with a color digital camera (various models) under transmitted light with 8-bit resolution, at low magnification with a pixel size ranging from 7.9 μm – 15 μm (see section 2.3). The red channel of the color images was used for all analyses for best correspondence to the 650 nm C-Rover wavelength. A set of 10-20, non-overlapping image tiles was collected for each sample. A value of atn_{Kd} was computed for each image pixel of each tile. However, unlike measurements of atn_c described above, multiple image timepoints were not available from which to compute $datn/dt$. Instead, we assumed that prior to particle accumulation, $I_d = I_o$ for each image pixel (that is, at time = 0, $atn_{Kd} = 0$ m^2 m^{-2}). To obtain a value of I_o for each pixel, we assumed that the background lighting characteristics stayed the same across the N images collected with the same camera and microscope setup (i.e., on the same cruise). If undeployed "blank" gel images were collected, these were used to provide the appropriate pixel-specific I_o values. If no blank gel images were available, then a composite background image was created from the sample images. Assuming a sufficiently large number of images with randomly located particles, the background pixel value ($I_o(I,j)$) was set equal to the brightest value for that pixel over the whole set of N images (Eq. 4).

$$I_o(i,j) = \max_N I_d(i,j,N) \qquad \text{(Eq. 4)}$$

Prior to calculating atn_{Kd}, each image tile was visually examined for artifacts such as bubbles, zooplankton that were likely to have actively entered the trap, and sample jar edges. Masks were created manually to eliminate these areas from further analysis. Then, atn_{Kd} images were calculated (Eq. 1) and an area-weighted mean atn_{Kd} value was computed over all tiles for each sample. Finally, the collection period of the sediment trap deployment was used as the time interval to compute F_{atnKd}.

2.2 Evaluation of beam transmissometers as OSTs

While beam transmissometers have seen the widest use as OSTs due to their commercial availability and ease of integration to autonomous sampling platforms, they were not designed for the purpose of intercepting and detecting relatively large sinking particles. We tested the degree of bias likely to arise through use of a transmissometer as an OST due to imperfect filtering of environmental artifacts and instrument noise, self-shading by the instrument housing, and undersampling of rare, large particles by an optical beam with a small cross-section.

2.2.1 Sensitivity tests of algorithm for determining Fatn_c from a beam transmissometer

While the basis for determination of the atn_c rate of change is straightforward, the process of filtering out instrumental noise and environmental artifacts, like spikes and rapid negative excursions in atn_c, has the potential to introduce bias. We performed a series of sensitivity tests on an artificial dataset to evaluate the performance of our algorithm for retrieving F_{atnc} from a beam transmissometer. Simulated data from a transmissometer OST were generated with different characteristics including F_{atnc} magnitude (0.01-0.69 $m^2\ m^{-2}\ d^{-1}$), constant vs. variable F_{atnc}, presence/absence of positive and negative excursions, and different levels of random instrument noise. The parameters of the F_{atnc} algorithm (the despiking and smoothing filter window width, and the threshold for identifying "negative jumps") and the overall averaging period were systematically varied to find the settings that resulted in the lowest RMSE (between "true" and retrieved F_{atnc}) over the largest range of input data characteristics. The parameters tested are shown in Table 1.

Table 1. Parameters tested in $Fatn_c$ retrieval algorithm[1]

Filter window (h)	Negative jump threshold ($m^2\ m^{-2}\ d^{-1}$)	Overall averaging period (d)
1	0	0.25
1.5	-0.005	0.5
2	**-0.05**	1
4	-0.5	2

[1] Parameter values shown in boldface are the optimized values.

2.2.2. Self-shading

The design of a transmissometer includes upper and lower pressure housings that respectively contain the source and detector optics. When vertically mounted as for OST use, the upper housing is above the detector window, so particles must be carried into the sampling volume by ambient turbulence in the water. Under quiescent conditions or with rapidly sinking particles, the upper housing is most likely to preclude particle collection, which we refer to here as "self-shading" (Estapa et al. 2017). Using a rough turbulence scaling estimate, Estapa et al. (2017) estimated that at a dissipation rate of $\epsilon = 10^{-9}\ m^2\ s^{-3}$ (a midrange value for the upper 1 km; Waterhouse et al. 2014) self-shading would begin to impact particles settling faster than 200 m d^{-1}, with greater effects on faster settling particles and at lower ϵ values. Estapa et al. (2017) concluded that the impact of self-shading was likely negligible in that study which sampled the upper 500 m in a subtropical gyre where POC flux was dominated by small, slowly-settling particles (Durkin et al. 2015). In the present study, we now reconsider the impact of transmissometer self-shading in more productive settings with faster-sinking particles, and at deeper depths with less turbulence.

To test the extent of self-shading, we created a simple, particle tracking model on top of the output from a publicly available, non-dimensional large-eddy simulation (LES) of a turbulent flow field (Li et al. 2008). We scaled the modeled, non-dimensional velocities output from the LES to a range of dissipation rates and kinematic viscosities that are characteristic of the ocean interior ($\epsilon = 10^{-11}$-$10^{-7}\ m^{-2}\ s^{-3}$ and $\nu = 0.87\text{-}1.6 \times 10^{-6}\ m^2\ s^{-1}$; Waterhouse et al. 2014). Twenty simulations with different ϵ and ν values were completed. Simulated particles (1000 per ϵ-ν

combination) were randomly assigned sinking speeds from a lognormal distribution ranging from 1-1000 m d^{-1}. These were released at random times and locations in the model and followed through time to generate sinking particle "tracks". Then, we generated a polyhedron representation of a C-Rover transmissometer (10 cm diameter) adjacent to a profiling float hull (15 cm diameter), and translated the particle tracks so that they all terminated within the transmissometer's beam cross section at the detector window. Using the MATLAB Central File Exchange function "inpolyhedron.m" (Sven 2023) we detected which simulated particle tracks intersected the transmissometer housing, and thus would have been affected by "self-shading". The fraction of shaded particles and the 2.5th, 25th, 50th, 75th, and 97.5th percentiles of their sinking speed distributions were tabulated and compared to the sinking speed distribution of the initial particle population.

2.2.3 Effect of sampling cross-section

The light beam in most commercial beam transmissometers has a relatively small cross section, generally on the order of 1 cm diameter where it intersects the detector window on which sinking particles accumulate. This is only 1-2 orders of magnitude larger than the sinking particles themselves, which have diameters on the order 100 µm – 1 mm in size. Thus, a transmissometer beam cross section is small enough that long averaging periods may be necessary to adequately characterize the true flux. We characterized the tradeoff between averaging period and sampling cross section by analyzing an image timeseries collected using an *in situ* camera sensor looking upwards through a polyacrylamide gel sediment trap. Particles larger than 300 µm were identified and tracked in the image timeseries, and then the "area flux" of particles (particle area per time) within subsampled areas of varying diameter (0.7-5 cm) was calculated and compared to the flux in the entire image (see section 3.2.3).

2.3. Data sets

To assess the empirical relationships among F_{atnc}, F_{atnKd}, and POC flux (F_{POC}), we compiled all available data sets that included F_{atnc}, F_{atnKd}, or both, as well as co-located F_{POC} from sediment trap measurements. Table 2 summarizes the key information chronologically, and sections 2.3.1-

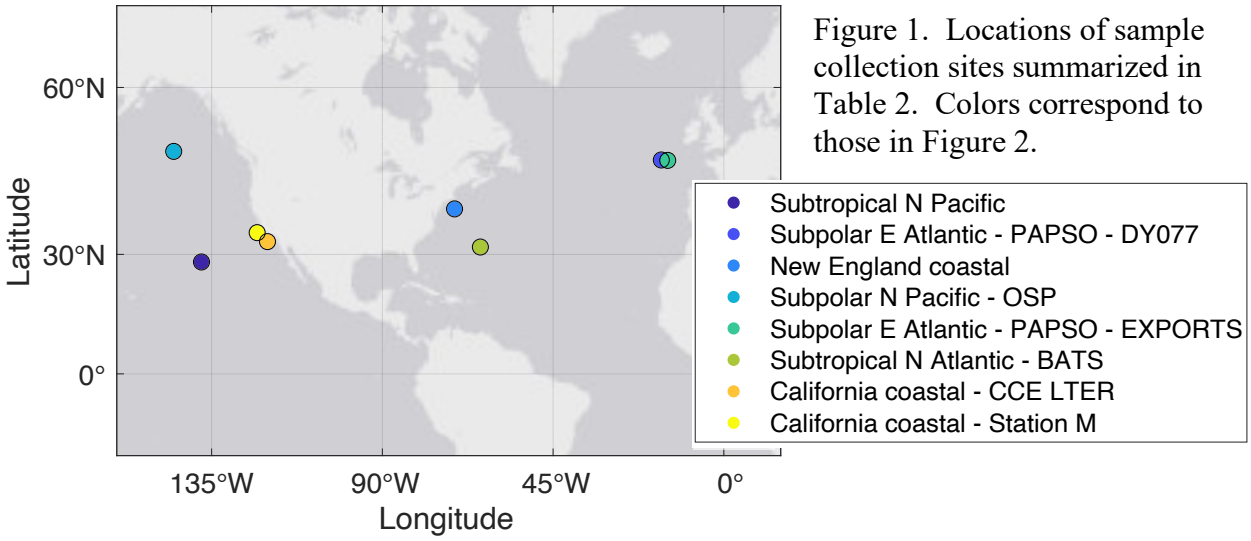

Figure 1. Locations of sample collection sites summarized in Table 2. Colors correspond to those in Figure 2.

2.3.8 briefly describe the details and deviations of each deployment. The mean geographic locations where the data were collected are summarized in Figure 1. As much as possible, we refer the reader to the original publications of these data sets for deployment, sample analysis details, and links to the original data, in order to minimize repeated information. Where new data are presented here for the first time, we provide an expanded description of these details. The individual measurements are available upon request from the author.

Table 2. Dataset summary

Region (Program)[1]	Year	References[2]	Position (degrees)	F_{atnc} method	F_{atnKd} method
Subtropical N. Atlantic (BATS)	2013-2014	1	31.67N -64.17E	C-Rover on NBST	Gel trap microscopy
California Coastal (Station M)	2014-2015	2,3	34.83N -123.00E	None	Sedimentation Event Sensor[3]
New England coastal	2015-2016	4,5	39.80N -70.97E	C-Rover on NBST	Gel trap microscopy
Subtropical North Pacific	2017	5,6	28.25N -137.68E	C-Rover on NBST	Gel trap microscopy
Subpolar NE Atlantic (PAPSO)	2017	4,7	48.98N -16.48E	C-Rover on NBST	Gel trap microscopy
California Coastal (CCE LTER)	2017	8,9	32.87N -120.28E	None	Carbon Flux Explorer[4]
Subpolar North Pacific (Station P-EXPORTS)	2018	6,10	50.45N -144.99E	C-Rover on NBST	Gel trap microscopy
Subpolar Northeast Atlantic (PAPSO-EXPORTS)	2021	6	48.92N -14.79E	C-Rover on NBST	Gel trap microscopy

[1] Program and site acronyms: BATS: Bermuda Atlantic Timeseries Study; PAPSO: Porcupine Abyssal Plain Sustained Observatory; CCE LTER: California Current Ecosystem Long Term Ecological Research; EXPORTS: Export Processes in the Ocean Through Remote Sensing.

[2] References: (1) Estapa et al. (2017); (2) Huffard et al. (2020); (3) McGill et al. (2016); (4) Estapa et al. (2019b); (5) Durkin et al. (2021); (6) *this study*; (7) Baker et al. (2020); (8) Bourne et al. (2019); (9) Bishop et al. (2016); (10) Estapa et al. (2021)

[3] Described in section 2.3.2
[4] Described in section 2.3.6

2.3.1. Subtropical N. Atlantic (BATS)

This site is an oligotrophic, subtropical gyre setting characterized by a low productivity, highly recycling ecosystem. Data were collected monthly from July-September (stratified period) and also just prior to the spring bloom (March). Sediment trap deployments and sample analyses are described by Estapa et al. (2017). The deployment depths spanned from 150-500 m. Key caveats are that the particulate carbon flux is from particles 350 μm and smaller due to the

screens used to remove zooplankton "swimmers", and total particulate carbon rather than POC was analyzed. However, passively sinking particles at this site were small, and the particulate inorganic carbon contribution to the flux tends to be negligible (Durkin et al. 2015; Estapa et al. 2017). Although polyacrylamide gel traps were deployed (Durkin et al. 2015), they were not imaged under transmitted light, so no atn_{Kd} estimates are available.

2.3.2. California Coastal (Station M)

This site underlies a productive, upwelling eastern boundary current system. Data were collected over the course of 8 months (October 2014-June 2015; Huffard et al. 2020). Measurements were made at a depth of 3,900 m, with POC fluxes collected in a moored, conical trap (Parflux, McLane, Inc.) and images of sinking particles measured *in situ* with the transmitted-light, imaging Sedimentation Event Sensor (SES) located 3.2 km from the sediment trap. The deployments, trap sample analyses, and SES instrument are described elsewhere (McGill et al. 2016; Huffard et al. 2020). The SES images (10.5281/zenodo.7613681) were reanalyzed here to provide estimates of F_{atnKd} using the "composite background" method described in section 2.1.2. In addition to POC fluxes, mass fluxes were also available from this deployment.

2.3.3. New England Coastal

This site is a productive near-coastal setting, with measurements collected in November (fall diatom bloom) and June (early summer, with flux dominated by zooplankton fecal matter). Sediment traps were deployed at a depth of 150 m, seaward of the shelf break current. These deployments and sample collections are described and links to the data are provided by Durkin et al. (2021). Gel sediment traps were imaged at a resolution of 15 μm/pixel.

2.3.4. Subtropical North Pacific

Sediment trap deployments were carried out at a depth of 150 m during two process stations in the subtropical North Pacific in wintertime, as part of the "Sea2Space" project (as described by Durkin et al. 2021). One station was representative of a low-productivity subtropical gyre setting, and the other was located in the productive California coastal current. The new F_{atnKd} estimates were derived from the transmitted light images of these samples (resolution 7.9 μm/pixel) published by Durkin et al. 2021.

2.3.5. Subpolar NE Atlantic (PAPSO)

Sediment trap deployments were carried out at depths of 200 and 350 m during a sediment trap intercomparison experiment conducted at the PAPSO site in the subpolar Northeast Atlantic, just prior to the spring bloom. The deployments and sample analyses are described by Baker et al. (2020). The transmitted-light microscopy on the gels was collected with a pixel size of 11.5 μm. In addition to POC fluxes, mass fluxes were also available from this project. Data from this project are available from Estapa et al. (2019a).

2.3.6. California Coastal (CCE LTER)

The measurements from this study were collected in the productive, upwelling California coastal current system, and descriptions of particle characteristics were given by Bourne et al (2021). The POC and atn_{Kd} flux data from this study are reported without modification from the original publication (Bourne et al. 2019), except for a change of logarithmic base to match the definition of atn_{Kd} used here. Observations were collected at approximately 150 m with an autonomous, drifting, imaging sediment trap ("Carbon Flux Explorer", Bishop et al. 2016). The in situ camera sensor aboard the CFE looked upward into the base of a conical sediment trap, and collected series of images over 25 min time intervals, interspersed with cleaning cycles prior to collection of background images. Unlike the other atn_{Kd} estimates reported here, a threshold was applied prior to taking the image average, so that pixels with $atn_{Kd} < 0.046$ were set to zero (Bourne et al. 2019).

2.3.7. Subpolar North Pacific (Station P, EXPORTS)

These observations were collected in a low-productivity, iron-limited "high nutrient low chlorophyll" subpolar gyre, with the low particle flux dominated by zooplankton products and episodic salp blooms (Durkin et al. 2021; Steinberg et al. 2023). The sediment trap deployments and sample analyses from this study are described by Estapa et al. (2021), and the data are available in Estapa and Durkin (2018a). The gel traps were imaged at a resolution of 7.9 μm/pixel. In this study, the sediment trap samples were subject to a heavy contamination by zooplankton "swimmers", which was difficult to eliminate during sample processing. A post-analysis, statistical correction was also performed (Estapa et al. 2021).

2.3.8. Subpolar North Atlantic (PAPSO, EXPORTS)

The data from this study, whose trap deployments captured a high-flux event associated with the termination of the North Atlantic spring diatom bloom, have not been previously published. Briefly, POC fluxes were measured with a combination of neutrally buoyant sediment traps (NBSTs; Estapa et al. 2020) and surface-tethered sediment traps. All traps carried polyacrylamide gels deployed and analyzed similarly to Durkin et al. (2021), while NBSTs also carried beam transmissometers (e.g., C-Rover 2000) used as OSTs as described by Estapa et al. (2020). Gels were imaged at a resolution of 7.9 μm/pixel. The sediment traps were deployed in three cycles, for 2-6 day periods at depths from 75-500 m in the center of an anticyclonic eddy near the PAPSO site during the EXPORTS North Atlantic field campaign (Johnson et al., *in prep*). The sampling procedures are described briefly here, but correspond closely to the more detailed methods described by Estapa et al. (2021), with the exception that a statistical correction for zooplankton swimmer contamination was not required. Trap tubes were cylinders with collection areas of 0.0113 m^2. Two tubes on each trap were used for POC flux measurements and were filled with 500 mL of 0.1% formaldehyde-poisoned,70 ppt brine overlain with filtered seawater. One tube on each trap carried a polyacrylamide gel collector overlain by filtered seawater. Upon retrieval, the two brine tubes were combined, samples were passed through 350 μm screens, the screens picked clean of zooplankton, and then the screen contents were washed back into the < 350 μm sample. Samples were then split on a custom rotary splitter (Lamborg et al. 2008). Splits for POC were filtered onto precombusted GF/F filters (Whatman), and dried until analysis. The GF/F filters were split gravimetrically and portions of three filters from each sample were analyzed for total C via combustion elemental analysis, and inorganic C via

coulometric titration. POC flux was computed as the difference between the total and inorganic fluxes. Sample splits for mass flux were filtered onto pre-tared polycarbonate membranes then dried and reweighed, until stable to within 0.01 mg, to determine the mass flux. Data from this study are available in Estapa and Durkin (2018b).

2.4. Models relating POC flux to attenuance flux

We tested several empirical models to predict POC flux and mass flux from F_{atnc} and F_{atnKd}, and to characterize the relationship between atn_c and atn_{Kd}. To first order, we expected a linear Beer's law relationship to apply, however the compiled dataset included fluxes spanning three orders of magnitude, with different particle types from biogeochemically contrasting settings, so the data were log-transformed prior to carrying out regression analyses (Eq. 5). Where errors in the x- and y- variables were comparable (e.g. between atn_c and atn_{Kd}) we also tested Type-II regression models, otherwise we used Type-I models.

$$F_{POC} = 10^{a_2} \times (F_{atn})^{a_1} \qquad [\text{mg-C m}^{-2}\ \text{d}^{-1}] \qquad \text{(Eq. 5)}$$

The performances of the different empirical models were evaluated through the Root-Mean-Squared-Error (RMSE) between the observations and the model, and through their correlation coefficients.

3. Assessment

3.1. Models predicting POC flux from attenuance flux

The global dataset supports the prediction of POC flux from F_{atnc} or image-mean F_{atnKd}, and the prediction of mass flux from F_{atnKd}. The regression coefficients and RMSE values for the models are provided in Table 3 and the model fits are plotted with the observations in Figure 2. There was more scatter in the F_{atnKd}-F_{POC} relationship compared to F_{atnc} (R^2 = 0.90 vs. 0.70, Table 3), but the F_{atnKd}-F_{POC} relationship showed more linearity than did F_{atnc}-F_{POC} (a_1 = 0.94 ± 0.18 vs. 0.77 ± 0.14; Table 3; Figure 2). The strongly linear relationship between F_{atnc} and F_{atnKd} (a_1 = 1.00 ± 0.09; R^2 = 0.94; Table 3; Figure 2) is consistent with theoretical expectations (see section 4.3). The performance of F_{atnKd} as a proxy for mass flux was stronger than that of F_{atnc} (RMSE = 199 vs. 291 mg m^{-2} d^{-1}).

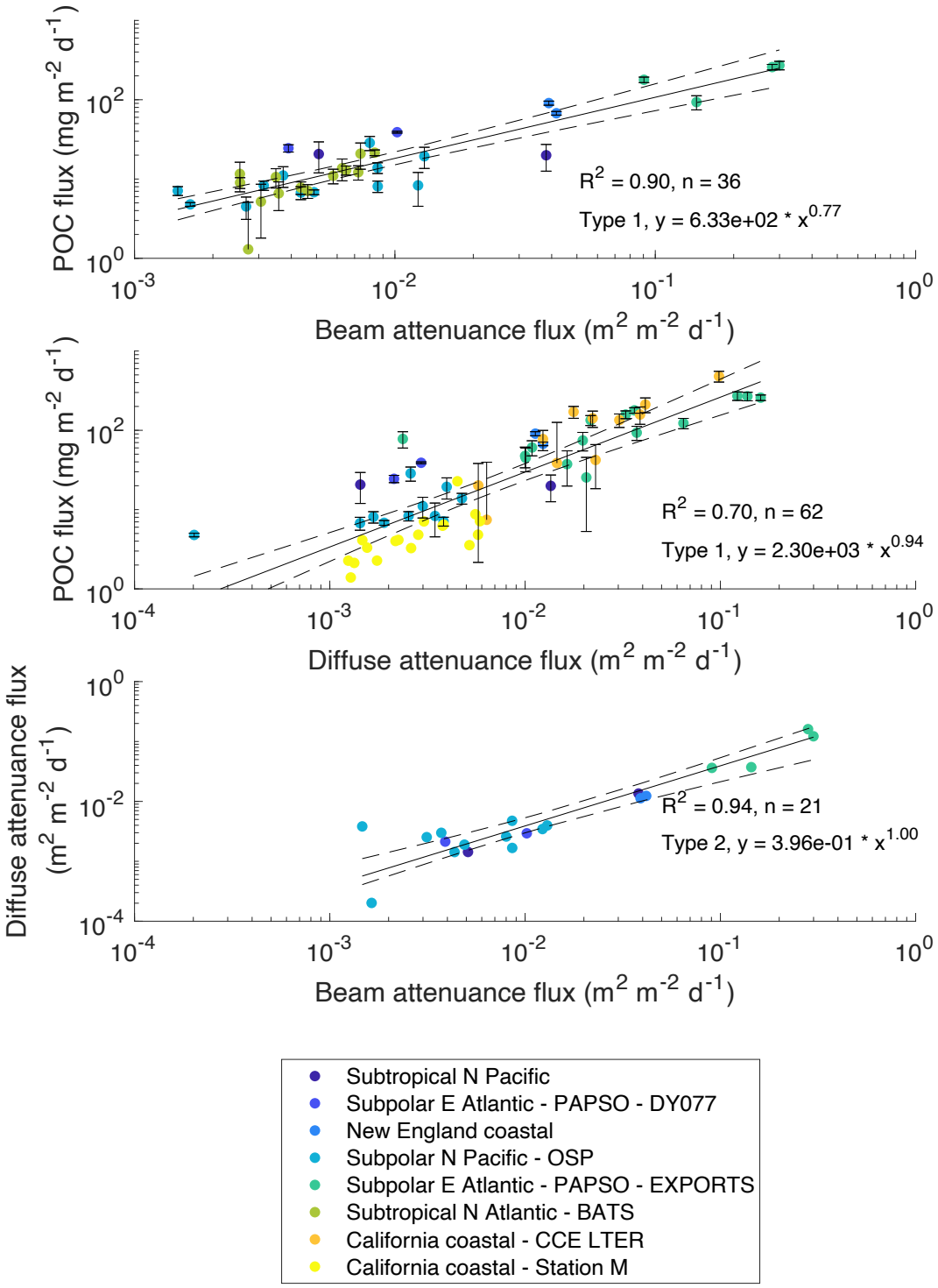

Figure 2. F_{POC} and *Fatn* flux models as compared to the data. Vertical error bars show uncertainty in F_{POC} observations. Solid line shows model fit to data and dashed lines show the 95% confidence interval of the fit. Best fit equations, R^2 values, and number of observations (n) are also given. Colors correspond to Fig. 1. Top) Prediction of F_{POC} from F_{atnc}. Middle) Prediction of F_{POC} from F_{atnKd}. Bottom) Relationship between F_{atnKd} and F_{atnc}.

Table 3. Summary of models tested, with coefficients as in Eq. 5.

x	y	Regression type	N	R^2	a_1 (unc)	a_2 (unc)	RMSE	Units for y and RMSE
$Fatn_c$	F_{POC}	1	36	0.90	0.77 (0.14)	2.8 (0.3)	19.38	mg-C m^{-2} d^{-1}
$Fatn_{Kd}$	F_{POC}	1	62	0.70	0.94 (0.18)	3.4 (0.4)	49.76	mg-C m^{-2} d^{-1}
$Fatn_c$	$Fatn_{Kd}$	1	21	0.94	0.93 (0.18)	-0.54 (0.36)	0.01729	m^2 m^{-2} d^{-1}
$Fatn_c$	$Fatn_{Kd}$	2	21	0.94	1.00 (0.09)	-0.40 (0.18)	0.01183	m^2 m^{-2} d^{-1}
$Fatn_c$	F_{mass}	1	7	0.77	0.65 (0.47)	3.4 (0.8)	291	mg m^{-2} d^{-1}
$Fatn_{Kd}$	F_{mass}	1	37	0.79	0.87 (0.16)	4.0 (0.4)	199	mg m^{-2} d^{-1}

3.2. Evaluation of beam transmissometer performance as an OST

The good correlation between F_{atnc} and F_{POC} suggests that biases due to algorithm assumptions, self-shading, and undersampling were at least consistent across the roughly three order-of-magnitude flux dataset analyzed here. The possible impacts of these biases were quantified through a series of modeling and sensitivity tests described below.

3.2.1 Sensitivity tests of the F_{atnc} data processing algorithm

The six simulated datasets, and the retrieval of F_{atnc} from them using the algorithm described in section 2.1.1 and by Estapa et al. (2017), are depicted graphically in Fig. 3. Two constant, mean $\delta atn_c/\delta t$ magnitudes were simulated, with and without spikes and jumps. A variable $\delta atn_c/\delta t$ at an intermediate magnitude was also simulated with and without spikes and jumps. Together, the six simulated datasets covered a $\delta atn_c/\delta t$ range of 0.01-0.69 m^2 m^{-2} d^{-1}. For each of the six simulated datasets, five different instrument noise levels were simulated, corresponding to noise standard deviations (SD) ranging from 0-8.6 × 10^{-3} m^2 m^{-2}. As a point of comparison, the manufacturer-reported precision of the 25-cm pathlength C-Rover 2000 used to collect the F_{atnc} data discussed here is c = 0.003 m^{-1}, equivalent to atn_c = 7.5 × 10^{-4} m^2 m^{-2}. In most cases when noise SDs were equal to or smaller than 8.6 × 10^{-4} m^2 m^{-2}, the algorithm was able to recover the original $\delta atn_c/\delta t$ to within 10% over the tested range and in the presence of large positive and negative "jumps" in the signal (noise SD of 8.6 × 10^{-4} m^2 m^{-2} case illustrated in Fig. 3). However, in the simulations with the highest noise level and the lowest $\delta atn_c/\delta t$, the true signal was not recoverable (Fig. 4). The algorithm's success at retrieving $\delta atn_c/\delta t$ was not especially sensitive to the negative jump threshold or to smoothing window widths ≤ 2 days, but was more sensitive to the relative instrument noise. This suggests that the most appropriate parameter choices will take into account the sensor-platform combination and how the OST is sampled and logged by the platform controller. For the simulated datasets used here, which mimicked the OST data collected by C-Rovers carried by NBSTs (Estapa et al. 2020), the optimal averaging

window length was 1.5 h and the optimal negative jump threshold was -0.05 $m^2\ m^{-2}\ d^{-1}$. The full results of all sensitivity tests are available from the authors upon request.

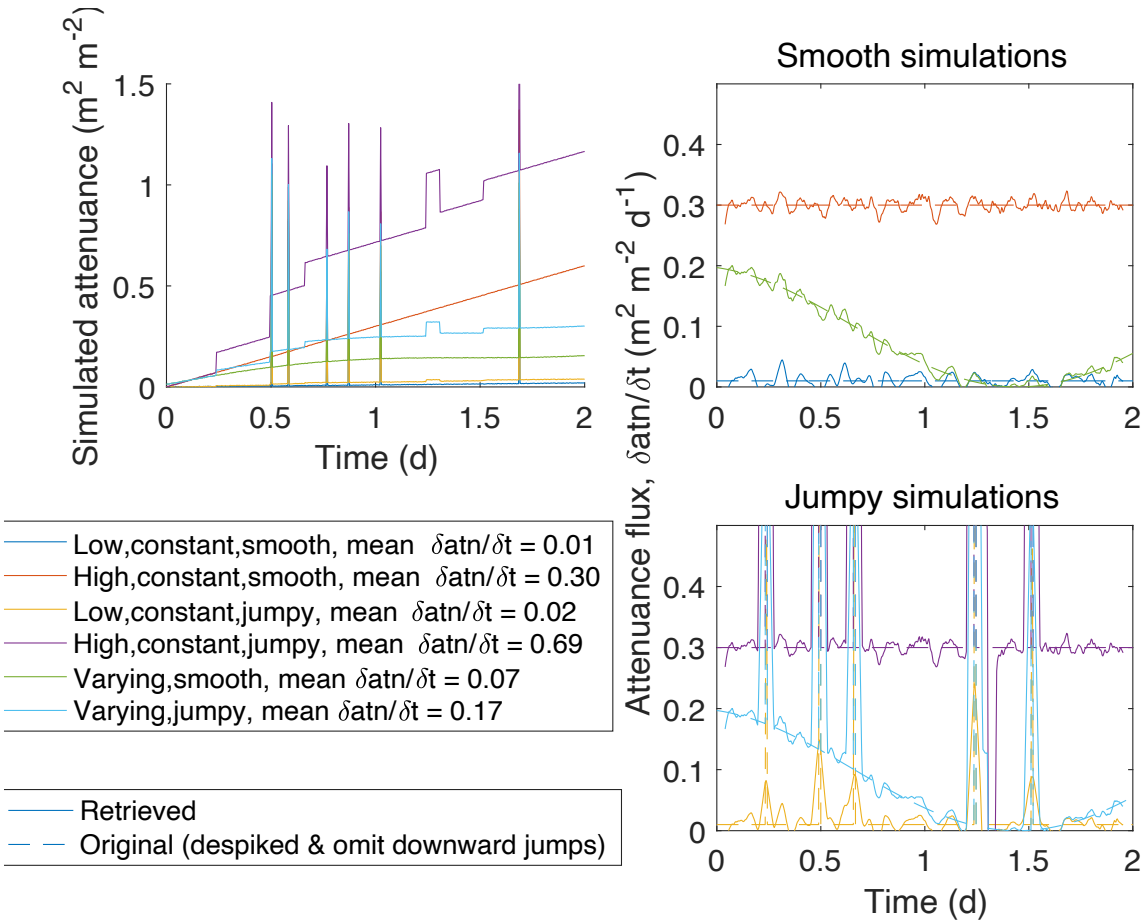

Figure 3. Simulated atn_c timeseries and ability of algorithm (section 2.1.1) to retrieve the atn_c rate of change ($\delta atn_c/\delta t$). Upper left panel: Original, simulated datasets with overall mean $\delta atn_c/\delta t$ values ($m^2\ m^{-2}\ d^{-1}$) shown in the legend. Upper right panel: Plots of $\delta atn_c/\delta t$ vs. time for simulated datasets without spikes and jumps (dashed lines) and the $\delta atn_c/\delta t$ retrieved using the algorithm described in section 2.1.1 (solid lines). Lower right panel: Same as upper right panel, only for the three datasets that included spikes and jumps. Timeseries shown here have added instrument noise with standard deviation of $8.6 \times 10^{-4}\ m^2\ m^{-2}$.

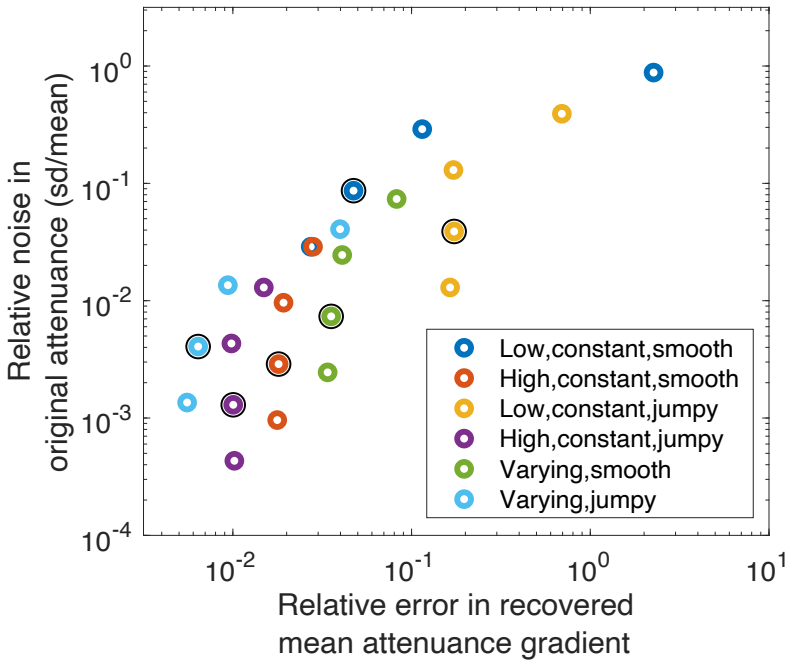

Figure 4. Relationship between the retrieved, mean $\delta atn_c/\delta t$ and the amount of instrument noise in the original attenuance signal (tested levels were 1, 3, 10, and 30 × 10^{-3} m^2 m^{-2}). Relative noise is expressed as the standard deviation of the noise divided by the mean attenuance in the original simulated data. Symbol colors and short legend labels correspond to the simulated datasets shown in Fig. 3, upper left panel. Symbols outlined in black correspond to the timeseries shown in Fig. 3 (noise SD of 0.003 m^2 m^{-2}).

3.2.2 Results of self-shading analysis

An example of sinking particle tracks simulated by the self-shading model is illustrated in Figure 5. The turbulent dissipation rate (ϵ) had a much greater effect on the extent of particle shading than did the viscosity (Fig. 6) so the results are summarized here as a function of ϵ only. As expected, there was more shading under lower-dissipation rate conditions, with 20-25% of particles blocked at $\epsilon = 10^{-11}$ m^2 s^{-3} but less than 5% blocked at $\epsilon \geq 10^{-8}$ m^2 s^{-3} (Fig. 6).

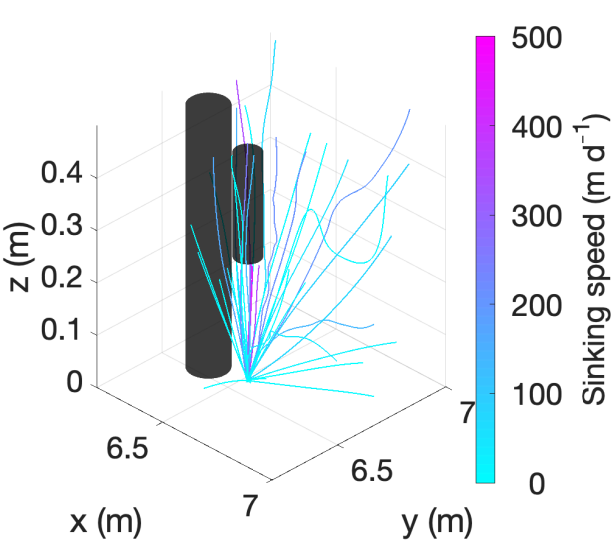

Figure 5. Illustration of model used to test extent of transmissometer self-shading. The large and small gray cylinders are the hulls of a profiling float and the upper housing of a transmissometer, respectively. Trajectories of sinking particles (colored lines; color denotes speed) were modeled at random locations in the turbulent velocity field and then translated to intersect the transmissometer's detector window.

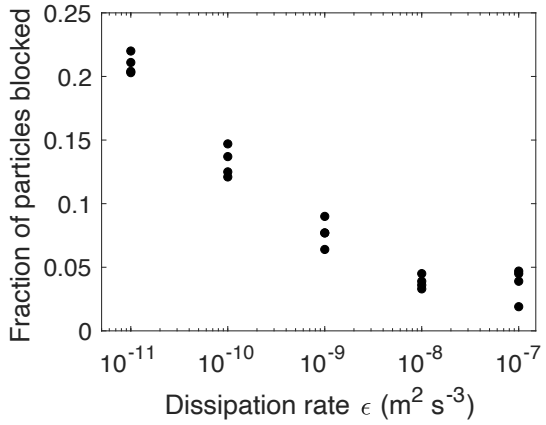

Figure 6. Fraction of particles blocked by the transmissometer or float hull as a function of dissipation rate. Scatter among points at each ϵ value represents the dependence upon kinematic viscosity (itself primarily a function of temperature), and was much smaller than the dependence on ϵ.

Also as expected, particles with faster sinking speeds were disproportionately shaded compared to slower-sinking particles. We compared the sinking speed distribution of the shaded particles to that of the whole modeled population and found that the shaded particles had higher sinking speeds (Fig. 7). For instance, the median sinking speed of the modeled particles was 29 m d^{-1},

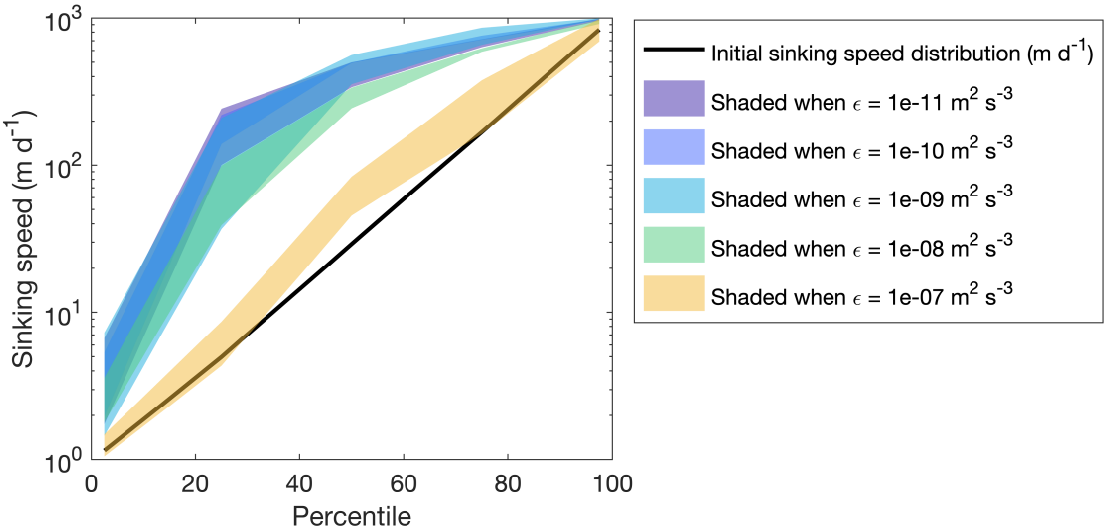

Figure 7. Comparison of sinking speed distributions of particles that were blocked by the transmissometer or float hull (colored, shaded patches) to the speed distribution of the initial particle population (black line). The turbulent dissipation rate ϵ is indicated by color. The vertical breadth of the colored areas is caused by differences due to kinematic viscosity and random variability (since the number of blocked particles was small).

while the median sinking speed of shaded particles ranged from 45-558 m d^{-1}. The sinking-speed dependence of shading was most pronounced at lower ϵ, whereas at the largest modeled value ($\epsilon = 10^{-7}$ m^2 s^{-3}), the distribution of shaded sinking speeds began to approach that of the initial population (Fig. 7).

3.2.3. Effect of optical sampling cross-section

In situ, time-lapse video imagery from a gel trap sample in the subtropical North Pacific dataset (section 2.3.4) allowed us to examine the choice of "beam" or imaged area on attenuence flux. The camera, mounted beneath the transparent bottom of the gel cup, took an image every 20 minutes, for a duration of 61 hours. Each 5 megapixel image was cropped to remove blurring and distortion, resulting in a 6.8 cm by 5.6 cm imaged area and a pixel size of approximately 50 μm (Figure 8). The smallest size of particle that could be resolved from the images had an equivalent spherical diameter of about 300 μm.

The fractional cross-sectional area occluded by particles was calculated for the entire imaged area (thick black line, Figure 8a-c), resulting in a timeseries that resembled the simulated attenuance shown in Figure 2. Next, each image was sub-sampled with different sizes of "beam diameter", with the smallest diameter (~0.7cm) corresponding to the beam of a C-Rover transmissometer (Fig. 8a). A Monte Carlo sampling approach was applied by randomly selecting the central position of each subsampled region, and generating a timeseries of fractional cross-sectional area covered by particles. These experiments were repeated ten times for each of the sub-sampled "beams". The means of these experiments (thin black lines, Figure 8a-c) and the standard deviations (gray shaded areas) show an expected increasing trend over time, with significantly larger stochasticity in the experiments with small beam diameter. The root mean square deviation (RMSD, Eq. 6; Figure 8d-f) was calculated from

$$RMSD^2 = \frac{\sum_{i=1}^{N}(atn_i - atn_{true})^2}{N} \qquad \text{(Eq. 6)}$$

and showed that as the simulated beam diameter increases, the results converge toward the case with the full imaged area (of 38 cm^2). Here, we found that >90% of the total variability was captured by a beam area greater than 5 cm^2. The results highlight that the discrete arrivals of large particles have a strong impact on the time variability of the area flux (and also of F_{atn}), particularly when the subsampled area is small.

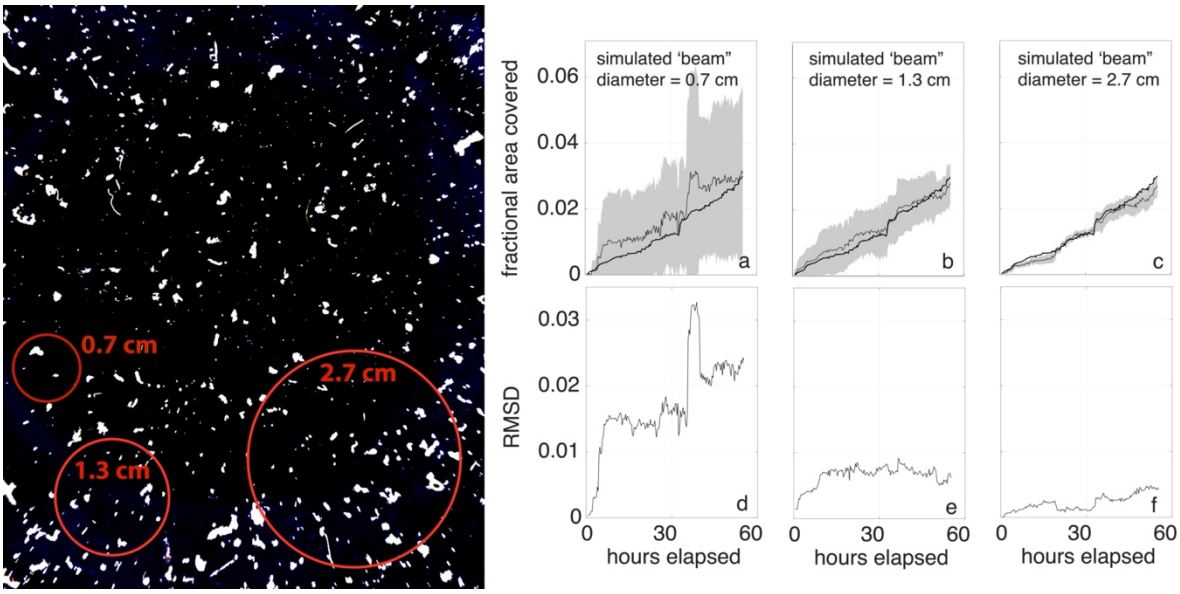

Figure 8. Effect of area sampled by an optical detector on flux signal variability. Left panel: An example of a processed image, with >300 µm particles shown in white. Red circles indicate the sizes of sub-sampled areas. Right panels: Time series of the fractional area occluded by particles over the entire image (thick black line), and arriving in 10 subsampled areas in random, non-overlapping locations, for a "beam" diameter of a) 0.7 cm, b) 1.3 cm, and c) 2.7 cm. The thin black line shows the mean of these 10 simulations, and gray shading indicates their standard deviation. Panels d) to f) show the corresponding root mean square deviation for each case.

4. Discussion

4.1 Attenuance flux as a quantitative proxy for POC flux

The importance of the ocean's biological carbon pump to global climate (Volk and Hoffert 1985), and its centrality to proposals to artificially enhance ocean biological carbon uptake (National Academies of Sciences, Engineering, and Medicine 2021), demand that we expand global observations of the gravitational carbon pump (GCP) in the highly undersampled waters below the mixed layer. To that end, proxies that can accurately quantify GCP fluxes from autonomous platforms, and without ship support, will be especially valuable (Claustre et al. 2021). Attenuance flux can be estimated through a variety of methods, all of which measure the light transmitted through accumulating, sinking particles. Many of these methods have been, or can be adapted for autonomous use.

Multiple prior studies have observed a correspondance between POC flux and *atn* flux in regional settings (Bishop et al. 2004, 2016; Bishop and Wood 2009; Estapa et al. 2013, 2017, 2019b; Bourne et al. 2019, 2021). This expected, quantitative relationship is analogous to Beer's Law which predicts that light attenuation will follow mass concentration in a water volume, although in the present application, attenuance and mass accumulation are measured in an area

rather than a volume. Here, we have confirmed this expectation, and shown that global, empirical models can respectively describe the POC:atn_c and POC:atn_{Kd} relationships across three orders of magnitude in flux and across contrasting ocean biogeochemical settings. Decreased uncertainty in the prediction can be achieved on a site-specific basis if appropriate calibration data are collected (for instance, see differences among sites in Fig. 2). Furthermore, the strong relationship between atn_c and atn_{Kd} observed here shows that measurements from different types of attenuance flux sensors can be quantitatively related to one another, facilitating meta-analyses across different studies.

4.2. Beam transmissometers as F_{atnc} sensors

The main advantage to the use of a beam transmissometer as an optical sediment trap is the ubiquity of the sensor, which has been commercially available for decades (e.g. C-Rover 2000 described previously; C-Star, Sea-Bird Scientific, Bellevue, Washington, USA; LISST-Tau, Sequoia Scientific, Bellevue, Washington, USA) and can be powered and sampled from commercially-available, autonomous platforms. While not one of the standard sensors on profiling floats in the global Biogeochemical-Argo program (Bittig et al. 2019), beam transmissometers have been more widely deployed than any other F_{atn} sensor to date (Bishop et al. 2004; Estapa et al. 2013, 2019b; Terrats et al. 2020). Even though there are clear issues stemming from the fact that transmissometers were never designed to operate as sediment traps, they are well-characterized and relatively easy to acquire and deploy, adding great value to the F_{atnc} data that these sensors continue to provide.

Because beam transmissometers are designed to measure the beam attenuation coefficient c in a water volume, they have characteristics that introduce bias when the sensor is instead employed as an optical sediment trap (OST). The primary issues stem from the small cross section of the light beam, and the upper pressure housing which blocks particles from sinking straight downward onto the detector window. The narrow beam cross section increases the time variability of the signal, and makes it more likely that accumulated particles will be dislodged in between samples leading to "negative jump" artifacts in the data. The algorithm that is used to process the raw atn_c vs. time data from a beam transmissometer-based OST must be tuned to eliminate these artifacts (section 3.2.1). In addition, averaging periods of multiple days may be needed to compensate for variability caused by discrete particle arrivals into a small sampling cross-sectional area (Fig. 8), which limits the utility of a transmissometer-OST for looking at high-frequency variability in the GCP. Each combination of sensor, platform, and sampling design (i.e., the frequency with which the transmissometer is sampled) should be coupled to a round of sensitivity tests of the data processing algorithm, to insure that the thresholds and averaging periods are tuned to the raw data characteristics.

The upper pressure housing of a beam transmissometer blocks a fraction of sinking particles from reaching the detector surface. The main controls on this are the ambient turbulence which moves particles sideways into the sensor volume, and the sinking speeds of the particles. Dissipation rates in the upper kilometer of the global ocean range conservatively from 10^{-11}–10^{-7} $m^2\ s^{-3}$, with the lower end of this range characterizing deep waters far from any boundaries, and the middle part of the range (10^{-10}-10^{-8} $m^2\ s^{-3}$) being more typical of the upper mesopelagic depths where GCP measurements are often made (Waterhouse et al. 2014; Whalen et al. 2015).

Under the lowest-ϵ conditions, at most about 23% of particles are shaded, with a bias against collection of the fastest-sinking particles. Even at $\epsilon > 10^{-8}$ m^2 s^{-3}, about 5% of particles will be shaded, although the sensitivity to particle speed diminishes (Fig. 7). Possible evidence for this in our observations is the departure from linearity of the relationship between F_{atnc} and F_{POC}, relative to F_{atnKd} and F_{POC} (Figure 2, Table 3). At higher F_{POC}, the relative decrease in the F_{atnc} response compared to F_{atnKd} is consistent with increasing self-shading at higher fluxes, assuming that particles sink faster when F_{POC} is higher. Although dissipation rate measurements are not routine during BCP studies, global compilations of ϵ estimates (e.g., Waterhouse et al. 2014; Whalen et al. 2015) should be consulted during study design to identify depths and regions where extra shading bias might impact F_{atnc} measurements from a transmissometer-OST.

The empirical atn_c*:POC* calibration provided here takes into account the biases of transmissometer-based attenuance flux measurements and provides POC flux estimates with uncertainties of approximately 19 mg-C m^{-2} d^{-1} (1.6 mmol-C m^{-2} d^{-1}), for deployments under conditions that are represented by the studies compiled here. The data used in the calibration were collected at depths ≤ 500 m, all with C-Rover 2000 transmissometers. Applications of this calibration to F_{atnc} observations collected at deeper depths away from boundaries may result in F_{POC} fluxes that are biased slightly low (due to more sensor self-shading under lower turbulence than is accounted for by the calibration). The uncertainty in the atn_c*:POC* flux calibration given here is large enough that transmissometer-derived flux estimates are best utilized in high-productivity, high-flux settings.

4.3. Diffuse attenuance flux from transmitted-light, imaging sensors

Transmitted-light imaging sensors can provide diffuse attenuance flux measurements that also perform well as a proxy for POC flux. Although the atn_{Kd}*:POC* calibration has higher uncertainty than the one based on atn_c, imaging sensors provide complementary, simultaneous observations of particle size and identity, and they tend to have larger collection areas than transmissometer-OSTs, which eliminates some of the temporal variability introduced by small beam cross sections. Carbon fluxes are often predicted from the analyzed images by assuming relationships among particle volume, carbon content, and composition (e.g., Durkin et al. 2021). In addition to these assumptions, the specific particle detection steps in the image analysis can introduce some uncertainty to the POC flux prediction (Giering et al. 2020b). POC flux prediction from F_{atnKd}, on the other hand, does not require particle detection or assumptions about particle properties, and thus can provide an important constraint for those more complex models.

In datasets where both were measured, we found that $Fatn_{Kd}$ was consistently lower than $Fatn_c$, with an atn_{Kd}/atn_c ratio of about 0.4 (Fig. 2, bottom panel). This is analogous to the general relationship between the beam and diffuse attenuation coefficients in the water column, where K_d approaches c as the light field becomes less diffuse (Mobley 2022). In fact, Gordon (1975) similarly predicted a K_d/c ratio of approximately 0.4 for typical oceanic particle scattering properties, under natural, diffuse light in the ocean. While the illumination and sensor light acceptance angles were not available for the variety of imaging systems represented in our atn_{Kd} datasets, the fact that we find a consistent atn_{Kd}/atn_c ratio here suggests that the cameras used to collect the data probably had fairly wide acceptance angles and illumination light sources were

diffuse. This also implies that the atn_{Kd}:*POC* calibration reported here should not be applied to measurements from imaging sensors with very different geometries such as those using side-scattered light (e.g., Underwater Vision Profiler; Picheral et al. 2010, 2022) or collimated light (e.g. Laser Optical Plankton Counter or In Situ Ichthyoplankton Imaging System; Checkley et al. 2008; Cowen and Guigand 2008).

4.4. Choosing the sample area for F_{atn} sensors

It makes intuitive sense that fluxes derived from a small sample area such as those on C-Rover transmissometers (~0.7 cm diam) are more sensitive to stochastic events such as the arrival (or loss) or large particles. By simulating expected attenuance timeseries from randomly selected sub-regions of a gel trap with a fairly large total imaged area (~ 15 cm^2) we showed that this sensitivity improves markedly as the "beam" area is increased. Since this analysis was performed for particles larger than 300 μm, we were not able to investigate results that include small particles. Assuming that smaller particles arrive steadily over time, they would have a buffering effect, reducing the overall sensitivity of the to episodic large particle arrivals. Thus, the image area required to adequately represent true particle variability is likely a inversely proportional to the slope of the particle size distribution.

4.5. Comments and Recommendations

The choice of imaging vs. non-imaging F_{atn} sensors will depend on a number of application-specific considerations, such as platform power and longevity, the need for ancillary particle size and identity information, and automated vs. manual data interpretation requirements. However, some universal considerations could help inform the design of future sensors for attenuance-based measurements of gravitational POC flux. Sensors that are unshaded from above will eliminate a key source of bias. The good relationship here between atn_c and atn_{Kd} suggests that a slightly oblique and/or diverging light source will still allow the precise determination of attenuance flux, and of POC flux with appropriate calibration data. Alternatively, self-shading can also be minimized by placing an attenuance sensor beneath a conical sediment trap where the light source occupies a minimal fraction of the collection area (such as the SES and CFE systems; sections 2.3.2 and 2.3.6; McGill et al. 2016; Bishop et al. 2016). However, such systems can be larger and more complex, perhaps not lending themselves to lower-cost, autonomous, mobile platforms. Finally, sampling areas of optimized optical sediment traps should be large enough to minimize the uncertainty in attenuance flux measured at higher time resolution.

5. Conclusion

There is a growing need for well-calibrated, autonomous measurements of POC flux in the ocean, which can support studies of the biological carbon pump's mechanisms, evolution under climate change, and impact on Earth's carbon cycle. Such measurements are also key components of any program that aims to enhance the ocean's carbon dioxide uptake by accelerating the biological carbon pump. We have shown that the beam attenuance flux is a quasi-inherent optical property that can be used as a quantitative proxy for POC flux, much in the same way that the beam attenuation coefficient predicts the POC concentration. This proxy

is based on a global calibration dataset spanning three orders of magnitude in flux, from a broad range of ocean biogeochemical settings. We have also showed how diffuse attenuance flux, obtained here from images of accumulated particles, is related to beam attenuance flux and also predicts POC and mass flux. The most ubiquitous source of attenuance flux data at present comes from beam transmissometers used as optical sediment traps, and here we have quantified their biases due to self-shading and a small beam cross section, to aid in the interpretation of their derived flux estimates. Finally, to aid in the broader use and development of optical POC flux sensors, we have outlined the key features that should be included in new sensor designs.

6. Acknowledgements

We are grateful to the NASA EXPORTS science team and the captain and crew of the *RRS* James Cook for making possible the collection of the new particle flux data presented here. Funding for this work came from many sources over a period of several years: the National Science Foundation (NSF) Chemical Oceanography program award OCE-1660012 (ME); the NSF Biological Oceanography program award OCE-1703664 (CD, ME, MO); the National Aeronautics and Space Administration (NASA) New Investigator Program award NNX14AM01G (ME); the NASA Ocean Biology and Biogeochemistry program awards 80NSSC17K0662 and 80NSSC21K0015 (ME, CD, MO); the Schmidt Ocean Institute (ME, CD, MO); the NSF Small Business Technology Transfer program award 2136735 (ME, WS); and the David and Lucile Packard Foundation (CD, CH).

7. References

Alkire, M. B., E. D'Asaro, C. Lee, and others. 2012. Estimates of net community production and export using high-resolution, Lagrangian measurements of O2, NO3−, and POC through the evolution of a spring diatom bloom in the North Atlantic. Deep Sea Research Part I: Oceanographic Research Papers **64**: 157–174. doi:10.1016/j.dsr.2012.01.012

Baker, C. A., M. L. Estapa, M. Iversen, R. Lampitt, and K. Buesseler. 2020. Are all sediment traps created equal? An intercomparison study of carbon export methodologies at the PAP-SO site. Progress in Oceanography **184**: 102317. doi:https://doi.org/10.1016/j.pocean.2020.102317

Bishop, J. K. B., M. B. Fong, and T. J. Wood. 2016. Robotic observations of high wintertime carbon export in California coastal waters. Biogeosciences **13**. doi:10.5194/bg-13-3109-2016

Bishop, J. K. B., and T. J. Wood. 2009. Year-round observations of carbon biomass and flux variability in the Southern Ocean. Global Biogeochemical Cycles **23**. doi:10.1029/2008GB003206

Bishop, J. K. B., T. J. Wood, R. E. Davis, and J. T. Sherman. 2004. Robotic Observations of Enhanced Carbon Biomass and Export at 55°S During SOFeX. Science **304**: 417–420. doi:10.1126/science.1087717

Bittig, H. C., T. L. Maurer, J. N. Plant, and others. 2019. A BGC-Argo Guide: Planning, Deployment, Data Handling and Usage. Frontiers in Marine Science **6**: 502. doi:10.3389/fmars.2019.00502

Bol, R., S. A. Henson, A. Rumyantseva, and N. Briggs. 2018. High-Frequency Variability of Small-Particle Carbon Export Flux in the Northeast Atlantic. Global Biogeochem. Cycles **32**: 1803–1814. doi:10.1029/2018GB005963

Boss, E., W. H. Slade, M. Behrenfeld, and G. Dall'Olmo. 2009. Acceptance angle effects on the beam attenuation in the ocean. Opt. Express **17**: 1535–1550.

Bourne, H. L., J. K. B. Bishop, E. J. Connors, and T. J. Wood. 2021. Carbon export and fate beneath a dynamic upwelled filament off the California coast. Biogeosciences **18**: 3053–3086. doi:10.5194/bg-18-3053-2021

Bourne, H. L., J. K. B. Bishop, T. J. Wood, T. J. Loew, and Y. Liu. 2019. Carbon Flux Explorer optical assessment of C, N and P fluxes. Biogeosciences **16**: 1249–1264. doi:10.5194/bg-16-1249-2019

Boyd, P. W., H. Claustre, M. Levy, D. A. Siegel, and T. Weber. 2019. Multi-faceted particle pumps drive carbon sequestration in the ocean. Nature **568**: 327–335. doi:10.1038/s41586-019-1098-2

Briggs, N., G. Dall'Olmo, and H. Claustre. 2020. Major role of particle fragmentation in regulating biological sequestration of CO_2 by the oceans. Science **367**: 791–793. doi:10.1126/science.aay1790

Briggs, N., M. J. Perry, I. Cetinic, C. Lee, E. D'Asaro, A. M. Gray, and E. Rehm. 2011. High-resolution observations of aggregate flux during a sub-polar North Atlantic spring bloom. Deep Sea Research Part I: Oceanographic Research Papers **58**: 1031–1039. doi:10.1016/j.dsr.2011.07.007

Cetinić, I., M. J. Perry, N. T. Briggs, E. Kallin, E. A. D'Asaro, and C. M. Lee. 2012. Particulate organic carbon and inherent optical properties during 2008 North Atlantic Bloom Experiment. Journal of Geophysical Research **117**. doi:10.1029/2011JC007771

Checkley, D. M., R. E. Davis, A. W. Herman, G. A. Jackson, B. Beanlands, and L. A. Regier. 2008. Assessing plankton and other particles in situ with the SOLOPC. Limnology and Oceanography **53**: 2123.

Claustre, H., L. Legendre, P. W. Boyd, and M. Levy. 2021. The Oceans' Biological Carbon Pumps: Framework for a Research Observational Community Approach. Front. Mar. Sci. **8**: 780052. doi:10.3389/fmars.2021.780052

Cowen, R. K., and C. M. Guigand. 2008. In situ ichthyoplankton imaging system (ISIIS): system design and preliminary results. Limnology and Oceanography: Methods **6**: 126–132. doi:https://doi.org/10.4319/lom.2008.6.126

Dall'Olmo, G., and K. A. Mork. 2014. Carbon export by small particles in the Norwegian Sea. Geophysical Research Letters **41**: 2921–2927. doi:10.1002/2014GL059244

De La Rocha, C. L., and U. Passow. 2007. Factors influencing the sinking of POC and the efficiency of the biological carbon pump. Deep Sea Research Part II: Topical Studies in Oceanography **54**: 639–658. doi:10.1016/j.dsr2.2007.01.004

Durkin, C. A., K. O. Buesseler, I. Cetinić, M. L. Estapa, R. P. Kelly, and M. Omand. 2021. A Visual Tour of Carbon Export by Sinking Particles. Global Biogeochem Cycles **35**. doi:10.1029/2021GB006985

Durkin, C. A., M. L. Estapa, and K. O. Buesseler. 2015. Observations of carbon export by small sinking particles in the upper mesopelagic. Marine Chemistry **175**: 72–81. doi:10.1016/j.marchem.2015.02.011

Estapa, M., K. Buesseler, and R. Lampitt. 2019a. Carbon, Nitrogen, biogenic silica, thorium-234, and mass fluxes from upper ocean sediment traps at the Porcupine Abyssal Plain Sustained Observatory (PAP-SO) site in the Northeast Atlantic Ocean during RRS Discovery cruise DY077 in April of 2017.doi:10.1575/1912/bco-dmo.765835.3

Estapa, M. L. 2023. Beam transmissometer optical sediment trap quality control software.doi:10.5281/ZENODO.7595966

Estapa, M. L., K. Buesseler, E. Boss, and G. Gerbi. 2013. Autonomous, high-resolution observations of particle flux in the oligotrophic ocean. Biogeosciences **10**: 5517–5531. doi:10.5194/bg-10-5517-2013

Estapa, M. L., K. Buesseler, C. A. Durkin, and others. 2021. Biogenic sinking particle fluxes and sediment trap collection efficiency at Ocean Station Papa. Elementa: Science of the Anthropocene **9**: 00122. doi:10.1525/elementa.2020.00122

Estapa, M. L., and C. A. Durkin. 2018a. EXPORTSNP. SeaWIFS Bio-optical Archive and Storage System (SeaBASS), NASA. doi:10.5067/SeaBASS/EXPORTS/DATA001

Estapa, M. L., and C. A. Durkin. 2018b. EXPORTSNA. SeaWIFS Bio-optical Archive and Storage System (SeaBASS), NASA. doi:10.5067/SeaBASS/EXPORTS/DATA001

Estapa, M. L., C. Durkin, K. Buesseler, R. Johnson, and M. Feen. 2017. Carbon flux from bio-optical profiling floats: Calibrating transmissometers for use as optical sediment traps. Deep Sea Research Part I: Oceanographic Research Papers **120**: 100–111. doi:10.1016/j.dsr.2016.12.003

Estapa, M. L., M. L. Feen, and E. Breves. 2019b. Direct Observations of Biological Carbon Export From Profiling Floats in the Subtropical North Atlantic. Global Biogeochemical Cycles **33**: 282–300. doi:10.1029/2018GB006098

Estapa, M. L., J. Valdes, K. Tradd, J. Sugar, M. Omand, and K. Buesseler. 2020. The Neutrally Buoyant Sediment Trap: Two Decades of Progress. J. Atmos. Oceanic Technol. **37**: 957–973. doi:10.1175/JTECH-D-19-0118.1

Giering, S. L. C., E. L. Cavan, S. L. Basedow, and others. 2020a. Sinking Organic Particles in the Ocean—Flux Estimates From in situ Optical Devices. Frontiers in Marine Science **6**: 834. doi:10.3389/fmars.2019.00834

Giering, S. L. C., B. Hosking, N. Briggs, and M. H. Iversen. 2020b. The Interpretation of Particle Size, Shape, and Carbon Flux of Marine Particle Images Is Strongly Affected by the Choice of Particle Detection Algorithm. Frontiers in Marine Science **7**: 564. doi:10.3389/fmars.2020.00564

Gordon, H. R., O. B. Brown, and M. M. Jacobs. 1975. Computed Relationships Between the Inherent and Apparent Optical Properties of a Flat Homogeneous Ocean. Appl. Opt. **14**: 417. doi:10.1364/AO.14.000417

Henson, S. A., C. Laufkötter, S. Leung, S. L. C. Giering, H. I. Palevsky, and E. L. Cavan. 2022. Uncertain response of ocean biological carbon export in a changing world. Nat. Geosci. **15**: 248–254. doi:10.1038/s41561-022-00927-0

Huang, Y., A. J. Fassbender, J. S. Long, S. Johannessen, and M. Bernardi Bif. 2022. Partitioning the Export of Distinct Biogenic Carbon Pools in the Northeast Pacific Ocean Using a Biogeochemical Profiling Float. Global Biogeochemical Cycles **36**. doi:10.1029/2021GB007178

Huffard, C. L., C. A. Durkin, S. E. Wilson, P. R. McGill, R. Henthorn, and K. L. Smith. 2020. Temporally-resolved mechanisms of deep-ocean particle flux and impact on the seafloor carbon cycle in the northeast Pacific. Deep Sea Research Part II: Topical Studies in Oceanography **173**: 104763. doi:10.1016/j.dsr2.2020.104763

Johnson, K. S., J. N. Plant, J. P. Dunne, L. D. Talley, and J. L. Sarmiento. 2017. Annual nitrate drawdown observed by SOCCOM profiling floats and the relationship to annual net community production. J. Geophys. Res. Oceans **122**: 6668–6683. doi:10.1002/2017JC012839

Lacour, L., N. Briggs, H. Claustre, M. Ardyna, and G. Dall'Olmo. 2019. The Intraseasonal Dynamics of the Mixed Layer Pump in the Subpolar North Atlantic Ocean: A Biogeochemical-Argo Float Approach. Global Biogeochemical Cycles. doi:10.1029/2018GB005997

Lamborg, C. H., K. O. Buesseler, J. Valdes, and others. 2008. The flux of bio-and lithogenic material associated with sinking particles in the mesopelagic “twilight zone” of the northwest and North Central Pacific Ocean. Deep Sea Research Part II: Topical Studies in Oceanography **55**: 1540–1563.

Li, Y., E. Perlman, M. Wan, and others. 2008. A public turbulence database cluster and applications to study Lagrangian evolution of velocity increments in turbulence. Journal of Turbulence **9**: N31. doi:10.1080/14685240802376389

McGill, P. R., R. G. Henthorn, L. E. Bird, C. L. Huffard, D. V. Klimov, and K. L. Smith Jr. 2016. Sedimentation event sensor: New ocean instrument for in situ imaging and fluorometry of sinking particulate matter. Limnology and Oceanography: Methods **14**: 853–863. doi:https://doi.org/10.1002/lom3.10131

Mobley, C., ed. 2022. The Oceanic Optics Book.doi:10.25607/OBP-1710

National Academies of Sciences, Engineering, and Medicine. 2021. A Research Strategy for Ocean-based Carbon Dioxide Removal and Sequestration.

Nicholson, D., S. Emerson, and C. C. Eriksen. 2008. Net community production in the deep euphotic zone of the subtropical North Pacific gyre from glider surveys. Limnology and Oceanography 2226–2236.

Picheral, M., C. Catalano, D. Brousseau, and others. 2022. The Underwater Vision Profiler 6: an imaging sensor of particle size spectra and plankton, for autonomous and cabled platforms. Limnology & Ocean Methods **20**: 115–129. doi:10.1002/lom3.10475

Picheral, M., L. Guidi, L. Stemmann, D. M. Karl, G. Iddaoud, and G. Gorsky. 2010. The Underwater Vision Profiler 5: An advanced instrument for high spatial resolution studies

of particle size spectra and zooplankton: Underwater vision profiler. Limnology and Oceanography: Methods **8**: 462–473. doi:10.4319/lom.2010.8.462

Siegel, D. A., K. O. Buesseler, M. J. Behrenfeld, and others. 2016. Prediction of the Export and Fate of Global Ocean Net Primary Production: The EXPORTS Science Plan. Frontiers in Marine Science **3**. doi:10.3389/fmars.2016.00022

Steinberg, D. K., K. Stamieszkin, A. E. Maas, and others. 2023. The Outsized Role of Salps in Carbon Export in the Subarctic Northeast Pacific Ocean. Global Biogeochemical Cycles **37**. doi:10.1029/2022GB007523

Sven. 2023. Inpolyhedron - are points inside a triangulated volume? https://www.mathworks.com/matlabcentral/fileexchange/37856-inpolyhedron-are-points-inside-a-triangulated-volume.

Terrats, L., H. Claustre, M. Cornec, A. Mangin, and G. Neukermans. 2020. Detection of Coccolithophore Blooms With BioGeoChemical-Argo Floats. Geophys. Res. Lett. **47**. doi:10.1029/2020GL090559

Volk, T., and M. I. Hoffert. 1985. Ocean carbon pumps: Analysis of relative strengths and efficiencies in ocean-driven atmospheric CO2 changes. *The Carbon Cycle and Atmospheric CO: Natural Variations Archean to Present*. American Geophysical Union. 99–110.

Waterhouse, A. F., J. A. MacKinnon, J. D. Nash, and others. 2014. Global Patterns of Diapycnal Mixing from Measurements of the Turbulent Dissipation Rate. Journal of Physical Oceanography **44**: 1854–1872. doi:10.1175/JPO-D-13-0104.1

Whalen, C. B., J. A. MacKinnon, L. D. Talley, and A. F. Waterhouse. 2015. Estimating the Mean Diapycnal Mixing Using a Finescale Strain Parameterization. Journal of Physical Oceanography **45**: 1174–1188. doi:10.1175/JPO-D-14-0167.1